A new operando surface restructuring pathway via ion-pairing of catalyst and electrolyte for water oxidation

Zhuang, Linzhou; Li, Zhiheng; Li, Mengran; Tao, Haolan; Mao, Xin; Lian, Cheng; Ge, Lei; Du, Aijun; Xu, Zhi; More Authors

DOI
10.1016/j.cej.2022.140071

Publication date
2023

Document Version
Final published version

Published in
Chemical Engineering Journal

Chemical Engineering Journal 454 (2023) 140071

Contents lists available at ScienceDirect

Chemical Engineering Journal

journal homepage: www.elsevier.com/locate/cej

A new *operando* surface restructuring pathway via ion-pairing of catalyst and electrolyte for water oxidation

Linzhou Zhuang [a,b,1], Zhiheng Li [b,1], Mengran Li [b,c,*], Haolan Tao [a], Xin Mao [d], Cheng Lian [a], Lei Ge [e], Aijun Du [d], Zhi Xu [a,*], Zongping Shao [f,g,*], Zhonghua Zhu [b,*]

[a] State Key Laboratory of Chemical Engineering, East China University of Science and Technology, Shanghai 200237, China
[b] School of Chemical Engineering, The University of Queensland, Brisbane 4072, Australia
[c] Department of Chemical Engineering, Faculty of Applied Sciences, Delft University of Technology, van der Maasweg 9, 2629 HZ Delft, the Netherlands
[d] Centre for Materials Science, Queensland University of Technology, George Street, Brisbane 4001, Australia
[e] Centre for Future Materials, University of Southern Queensland, Springfield Central, QLD 4300, Australia
[f] Department of Chemical Engineering, Curtin University of Technology, Perth 6845, WA, Australia
[g] State Key Laboratory of Materials-Oriented Chemical Engineering, College of Chemical Engineering, Nanjing Tech University, Nanjing 211816, China

ARTICLE INFO

Keywords:
Operando surface restructuring
Strontium ion leaching
Cation size-matching
Oxygen evolution
Non-acidic medium

ABSTRACT

The highly efficient and stable electrolysis needs the rational control of the catalytically active interface during the reactions. Here we report a new *operando* surface restructuring pathway activated by pairing catalyst and electrolyte ions. Using $SrCoO_{3-\delta}$-based perovskites as model catalysts, we unveil the critical role of matching the catalyst properties with the electrolyte conditions in modulating catalyst ion leaching and steering surface restructuring processes toward efficient oxygen evolution reaction catalysis in both pH-neutral and alkaline electrolytes. Our results regarding multiple perovskites show that the catalyst ion leaching is controlled by catalyst ion solubility and anions of the electrolyte. Only when the electrolyte cations are smaller than catalyst's leaching cations, the formation of an outer amorphous shell can be triggered via backfilling electrolyte cations into the cationic vacancy at the catalyst surface under electrochemical polarization. Consequently, the current density of reconstructed $SrCoO_{3-\delta}$ is increased by 21 folds compared to the pristine $SrCoO_{3-\delta}$ at 1.75 V vs reversible hydrogen electrode and outperforms the benchmark IrO_2 by 2.1 folds and most state-of-the-art electrocatalysts in the pH-neutral electrolyte. Our work could be a starting point to rationally control the electrocatalyst surface restructuring via matching the compositional chemistry of the catalyst with the electrolyte properties.

1. Introduction

Oxygen evolution reaction (OER) is an enabling step for most of the key electrochemical applications such as hydrogen production, CO_2 electrolysis, and energy storage [1]. The interface between catalyst and electrolyte (or membrane) is at the heart of the OER catalysis, and plays a pivotal role in determining the activity, selectivity, and stability of the electrochemical systems [2]. However, these catalysts are usually unstable under oxidation potentials, and are subject to dynamic surface restructuring during the reactions [3,4]. This *operando* surface restructuring process has a profound impact on the overall reaction system [5–7].

Recent studies are sought to take advantage of such surface reconstruction phenomena to boost the OER activity by tuning the compositional chemistry of metal oxides [8]. The most common strategy is to incorporate electrolyte-soluble ions into the metal oxide lattice, such as alkali (e.g., Li^+) [9], alkaline-earth (e.g., Sr^{2+} and Ba^{2+}) [10,11], Al^{3+} cations [12], and halide anions (e.g., Cl^-) [13]. Under oxidation potentials, the dissolution of these cations or anions from the catalysts causes significant surface reconstruction to form an OER-active surface layer consists of catalytically-active phases (e.g., cobalt oxyhydroxide [3] in cobalt oxides) and lattice vacancies [14]. However, there are also reports raising concerns of the cation dissolution and anode restructuring that could also cause rapid cell failure in the application of CO_2

* Corresponding authors State Key Laboratory of Chemical Engineering, East China University of Science and Technology, Shanghai 200237, China (M. Li) Department of Chemical Engineering, Curtin University of Technology, Perth 6845, WA, Australia (Z. Shao).
E-mail addresses: m.li-8@tudelft.nl (M. Li), zhixu@ecust.edu.cn (Z. Xu), zongping.shao@curtin.edu.au (Z. Shao), z.zhu@uq.edu.au (Z. Zhu).
[1] These authors contributed equally to this work.

https://doi.org/10.1016/j.cej.2022.140071
Received 14 July 2022; Received in revised form 4 October 2022; Accepted 24 October 2022
Available online 29 October 2022

electrolysis [15], where the local reaction environment (e.g., (bi)carbonate cross-over from the cathode to the anolyte) is drastically different from water electrolysis. This discrepancy originates from the negligence of the electrolyte's role in determining the overall reaction reactivity and stability [16]. The catalytic process and surface restructuring process should depend both on the catalyst properties and potentials and their local reaction environment, such as electrolyte compositions and local pH, which remain poorly understood by far [17].

Hence, this work seeks to study the roles of electrolyte ions and catalyst compositions in the catalyst ion leaching and surface restructuring process during OER catalysis in a non-acidic medium, mostly in a pH-neutral electrolyte. We chose $SrCoO_3$ perovskite (SC) as the model anode catalyst and phosphate buffer solutions (PBS) as the main model electrolytes. The perovskites are emerging cost-effective alternatives to precious metals for the OER catalysis [18], while the PBS-electrolytes with a neutral *pH* have the potential to minimize the potential corrosions in the electrolyzers [19,20]. We chose PBS as the model electrolyte mainly because of the phosphate anions are different from hydroxide ions [21,22] and allow us to explore the impacts of anions on the catalyst surface restructuring and reactivity. Our experimental results confirm that the catalyst surface restructuring process during OER in varied electrolytes takes place involving ion leaching, electrolyte cation backfilling and anion incorporation. This restructuring process is closely related to the solubility of the cations of the metal oxides, the sizes of the ions of catalyst and electrolyte, and buffering capacity of the electrolyte anions. Consequently, an amorphous surface shell structure can be formed covering the Sr-containing perovskite core in the presence of Na^+-PBS electrolytes after anodic conditioning. The shell structure contains more oxygen vacancies that strengthen binding with oxygen intermediates and phosphate ions that promote proton transfer, so as to exhibit significantly enhanced OER activity in pH-neutral electrolyte and in alkaline medium.

2. Experimental

2.1. Materials preparation

The solid-state preparation method was applied to synthesize the catalysts, including $SrCoO_{3-\delta}$ (SC), $BaCoO_{3-\delta}$ (BC), $LaCoO_{3-\delta}$ (BC), $La_{0.5}Sr_{0.5}Co_{0.8}Fe_{0.2}O_{3-\delta}$ (LSCF), $Ba_{0.5}Sr_{0.5}Co_{0.8}Fe_{0.2}O_{3-\delta}$ (LSCF), $SrNb_{0.1}Ta_{0.1}Co_{0.8}O_{3-\delta}$ (SNTC) and $SrSc_{0.175}Nb_{0.025}Co_{0.8}O_{3-\delta}$ (SSNC). Stoichiometric mixtures of Co_3O_4 (Aldrich, ≥99.5 %), $SrCO_3$ (Aldrich, ≥99.9 %), $BaCoO_3$ (Aldrich, ≥99.98 %), La_2O_3 (Aldrich, ≥99.9 %), Nb_2O_5 (Aldrich, ≥99.99 %) and Ta_2O_5 (Alfa Aesar, ≥99.0 %) were weighed and ball-milled at 260 rpm for 20 h. Then the samples were dry-pressed in a die under 90 MPa and sintered at 1200 °C for 20 h. Finally, the sintered tablets were crushed into powders through ball-milling at 350 rpm for 8 h. As the SC powders were prepared via solid-state method and ground through ball-milling, their sizes may vary widely. Thus, the as-prepared SC powders were dispersed in ethanol via ultrasonication for 1 h, and centrifuged at the rotation speed of 1000 rpm. The supernatant was collected and dried under vacuum overnight to obtain the SC-origin with monodispersed particle size.

$La_{0.6}Sr_{0.4}CoO_{3-\delta}$ (LSC) and $La_{0.6}Sr_{0.4}MnO_{3-\delta}$ (LSM) were purchased from Fuel Cell Materials, whose particles size is 0.4–0.8 μm and 0.4–1.0 μm, respectively.

To prepare the 1.0 M sodium phosphate buffer solution (Na^+-PBS), 15.6 g sodium phosphate monobasic dehydrate ($NaH_2PO_4{\cdot}2H_2O$, Aldrich, ≥99.0 %) was dissolved in 100.0 mL deionized water, and denoted as solution A. Meanwhile, 28.4 g sodium phosphate dibasic heptahydrate ($Na_2HPO_4{\cdot}7H_2O$, Aldrich, ≥98.0 %) was dissolved in 200.0 mL deionized water, and denoted as solution B. Then 97.5 mL of solution A was mixed with 152.5 mL of solution B to obtain the 250 mL of Na^+-PBS. Its pH was tested to be 6.65.

To prepare the 1.0 M potassium phosphate buffer solution (K^+-PBS), 13.6 g potassium phosphate monobasic (KH_2PO_4, Aldrich, ≥99.0 %) was dissolved in 100.0 mL deionized water, and denoted as solution A. Meanwhile, 24.2 g potassium phosphate dibasic heptahydrate ($K_2HPO_4{\cdot}3H_2O$, Aldrich, ≥98.0 %) was dissolved in 200.0 mL deionized water, and denoted as solution B. Then 97.5 mL of solution A was mixed with 152.5 mL of solution B to obtain the 250 mL of K^+-PBS. Its pH was tested to be 6.62. To prepare the 1.0 M sodium sulfate solution (Na_2SO_4), 35.51 g anhydrous Na_2SO_4 was dissolved in 250 mL deionized water. Its pH was tested to be 7.18.

2.2. Catalyst reconstruction

10.0 mg active catalyst and 10.0 mg carbon black were dispersed in 1.0 mL ethanol with 100 μL 5 wt% Nafion solution through ultrasonication for 30 min. Then 400 μL of the obtained ink was loaded on the Ni foam (1 cm × 2 cm) to achieve the loading amount of 1.67 mg cm^{-2}, and dried under vacuum overnight. To carry out the catalyst reconstruction process, the continuous potentiometry *V*-t treatment was employed under a constant current density of 3.0 A g^{-1} for 40000 s.

2.3. Materials characterization

The reconstructed catalysts were stripped from the Ni foam through ultrasonication with ethanol for 20 min and then dried under vacuum overnight for characterization. High-resolution transmission electron microscope (HR-TEM, Tecnai F20), with energy dispersive spectrometer (EDS) mapping details of Sr, Co, and O elements, were applied to study the morphologies of the materials at a voltage of 200 kV. The line scan spectra of as-prepared SC and reconstructed SC were collected on the HF5000 Cs-TEM at the accelerating voltage of 80 kV. X-ray diffraction (XRD) patterns (2θ, 10–70°) were recorded on a Bruker D8-Advanced X-ray diffractometer with the nickel-filtered Cu-Kα radiation. The different electrodes were immersed in the various electrolytes, including Na^+-PBS (1.0 M), K^+-PBS (1.0 M), Na_2CO_3/$NaHCO_3$ (1.0 M), and Na_2SO_4 (1.0 M), and the anodic conditioning was then conducted for a certain period. Subsequently, the electrolytes were collected and sent for ICP analyses. The concentrations of their ions were analyzed with a Varian Vista Pro ICP-OES instrument. Co *K*-edge XAS spectra of all samples were recorded on at BL14W1 station in Shanghai Synchrotron Radiation Facility (SSRF). The beam energy was 3.0 GeV and the maximum beam current was 400 mA. The FTIR spectra were obtained by a PerkinElmer Spectrum 100 FT-IR spectrometer.

3. Results and discussion

3.1. Surface reconstruction of SC oxide in Na^+-PBS solutions

In 1.0 M Na^+-PBS solution, high-resolution transmission electron micrographs (HR-TEM) of SC manifest that a surface restructuring process took place during the electrochemical anodic conditioning at 3.0 A/g for 10 min, 40 min, 6 h, and 12 h (Fig. 1a–1e), respectively. The bulk core of SC could sustain its high crystallinity after conditioning treatment in neutral solution, which is confirmed by the distinguishable lattice fringes in HR-TEM images with a lattice spacing of 0.277 nm that corresponds to (0 1 1) lattice of cubic perovskite phase of SC [23,24]. The sustained structural integrity of SC is also confirmed by its X-ray diffraction (XRD) patterns before and after conditioning (Fig. S1) [25,26]. In contrast, the amorphous surface shell of the SC becomes thicker when the anodic conditioning duration increases, with an average thickness of the amorphous region increasing from 5.0 ± 0.3 nm for 10 min treatment to about 35.0 ± 1.0 nm for 12 h treatment. The thickness of the shell structure increases quickly at the first 6 h treatment and gradually slows down in the next 6 h (Fig. 1f). The slowing down of restructuring should be ascribed to the steric hindrance of the thick shell that prevents further penetration of electrolyte to the SC core when the shell structure is thick.

Analysis of energy-dispersive X-ray spectroscopy (EDS) line scans

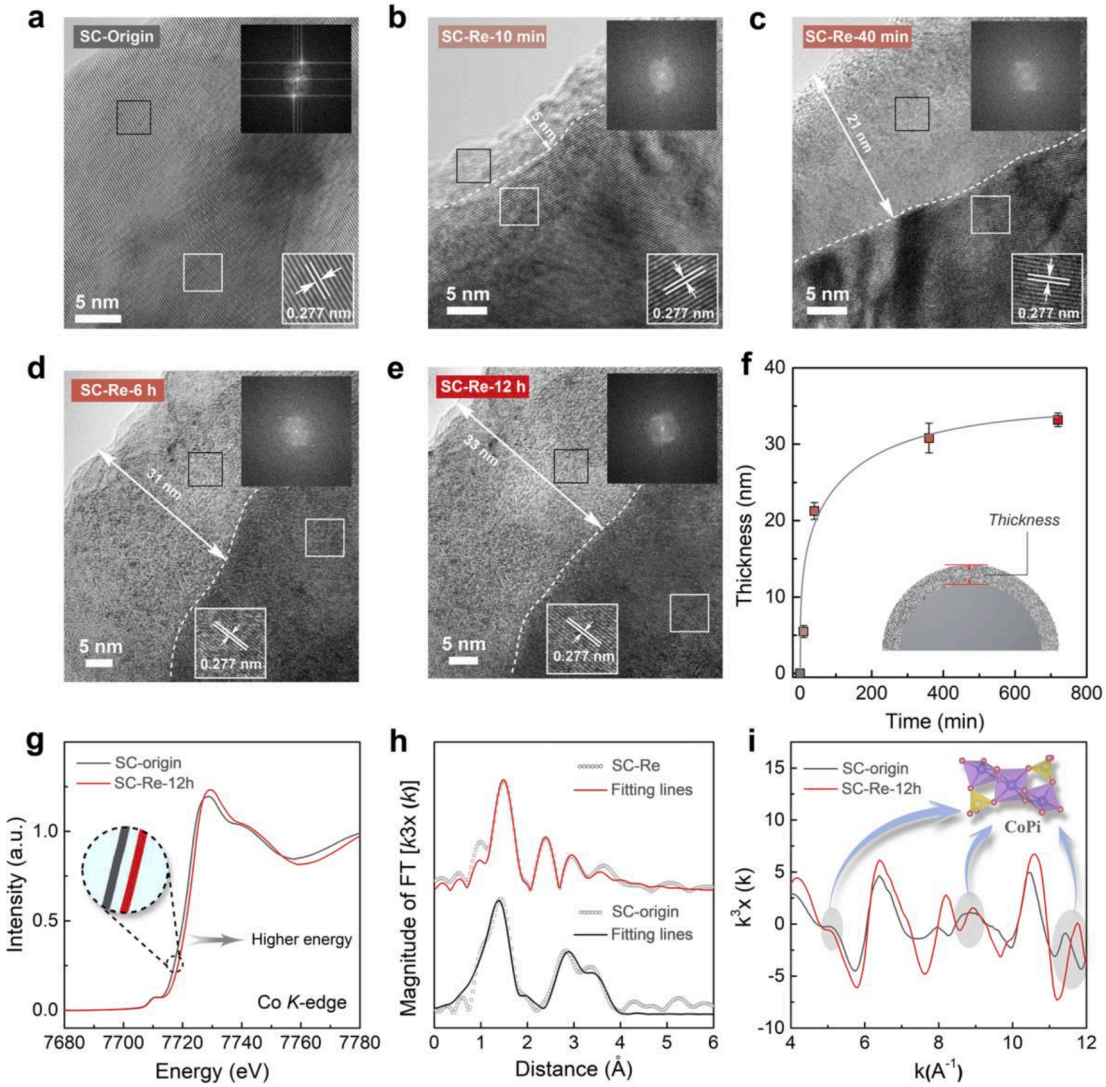

Fig. 1. (a–e) HRTEM images of SC-origin (a), SC-re-10 min (b), SC-re-40 min (c), SC-re-6 h (d) and SC-re-12 h (e), the upper inset images show the fast Fourier transforms (FFTs) of the selected area (4 nm × 4 nm), and the bottom inset images show the lattice fringe of the SC samples; (f) the average thickness of the amorphous region of SC that plotted to show its correlation with anodic restructuring duration; (g) Co *K*-edge XANES spectra for SC-origin and SC-re-12 h; (h) the k^3-weighted Fourier transform EXAFS spectra of SC-origin and SC-re-12 h and the fitting; (i) Co K-edge extended XANES oscillation functions $k^3\chi(k)$.

over SC oxides before and after 12-h treatment suggests a notable decrease of Sr/Co atomic ratio but an increase of phosphorus (P) content near the surface shell (Fig. S2), meeting well with the X-ray photoelectron spectroscopy (XPS) data (Fig. S3). X-ray absorption spectroscopy (XAS) was applied to investigate the relatively thick shell structure to reveal the chemistry of the catalyst restructuring process. Cobalt *K*-edge of the X-ray absorption near edge structure (XANES) spectrum of the 12 h-treated SC oxide shifts to a higher energy by nearly 1.0 eV as compared to the original SC (Fig. 1g), indicating that the cobalt ions would be oxidized during treatment [22,27]. When fitting the Fourier-transformed extended X-ray absorption fine structure (EXAFS) spectra against $SrCoO_3$ model [28], we find that the coordination number is reduced by 4.0 for the first cobalt-strontium shell and by 0.5 for the first cobalt-oxygen shell in the SC lattice (Fig. 1h and Table S1). The reduced coordination number indicates loss of strontium atoms in the lattice after the anodic conditioning, which is consistent with the EDS line analysis result (Fig S2). We also observe the formation of cobalt-phosphate bonds in SC oxides after 12 h treatment from the k^3-weighted EXAFS spectra particularly at $k = 5.0$ Å^{-1}, 8.5 Å^{-1}, and 11.5 Å^{-1} (where k represents photoelectron wavenumber, Fig. 1i) [29]. The formation of second cobalt-oxygen shell and cobalt-phosphate shell as observed from the EXAFS analysis further confirm the incorporation of phosphate into the SC lattice from the electrolyte solution. Moreover, FTIR results reveal a stronger broad characteristic peak at 1230 cm^{-1} for the typical vibrational and bending modes of phosphate when the anodic treatment duration increases (Fig. S4) [20]. The amorphous surface shell should be the region where the restructuring takes place, involving cobalt oxidation, loss of strontium cations, and phosphate incorporation.

3.2. OER performance improvement due to surface restructuring

The surface restructuring significantly improves the OER activity of SC in 1.0 M Na^+-PBS. The linear sweep voltammograms presented in Fig. 2a show that the mass-specific OER current densities increase with the conditioning durations. Specifically, the current densities at 1.75 V versus reversible hydrogen electrode (vs RHE) increased rapidly in the first 40 min treatment and then further to 31.4 A g^{-1} after 12 h treatment (Fig. 2b and Fig. S5). From the TEM-EDX mapping images, the homogeneous distribution of the ions in SC-Re could be confirmed (Fig. S6). We further carried out the *in situ* EIS test to study the charge-transfer ability of SC during the anodic conditioning. From Fig. S7 it can

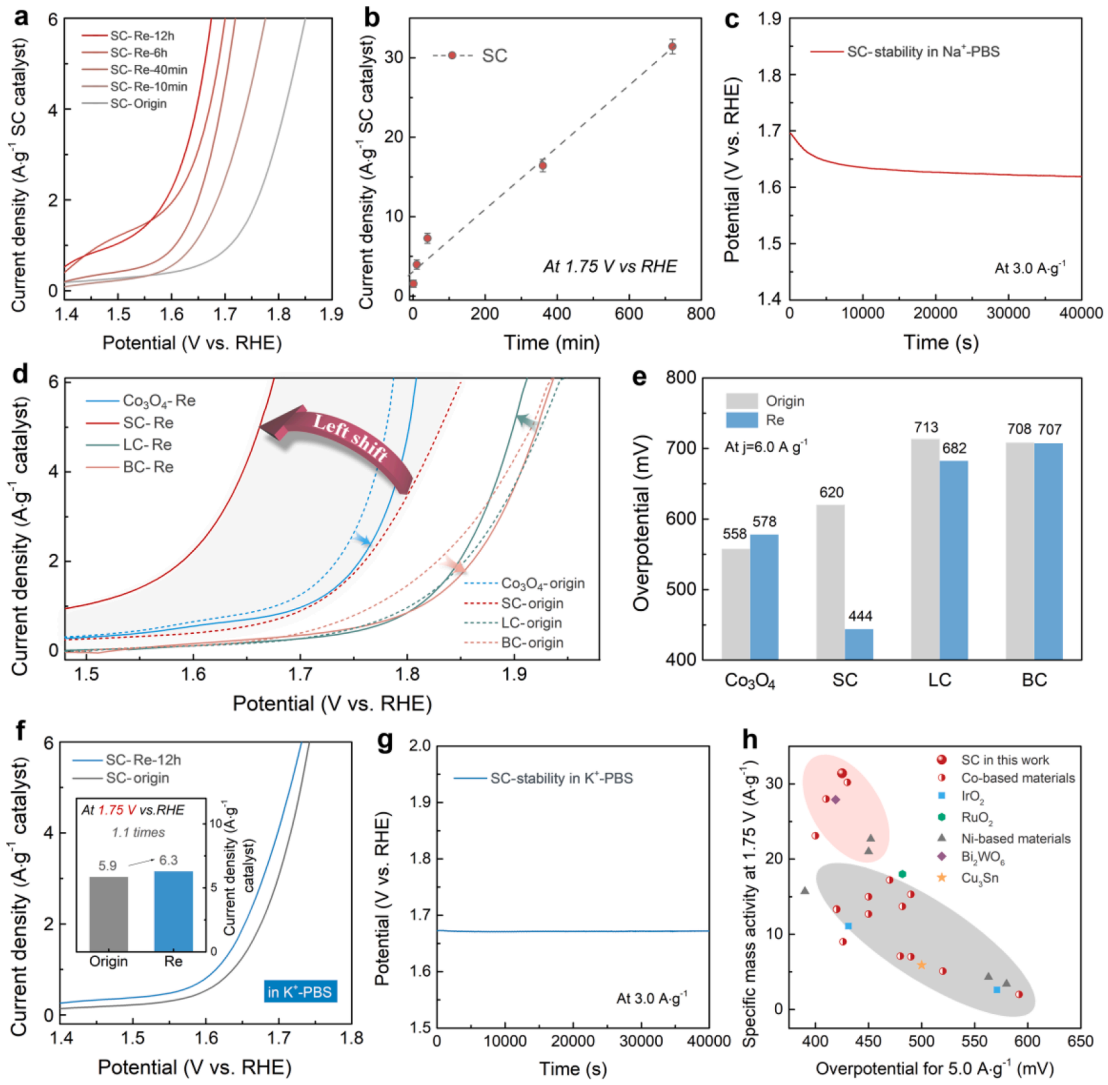

Fig. 2. (a) OER polarization curves of SC-origin, SC-re-10 min, SC-re-40 min, SC-re-6 h, and SC-re-12 h; (b) OER current density of SC-Re at 1.75 V vs RHE that plotted to show its correlation with anodic restructuring duration; (c) Continuous potentiometric V-t measurement of SC at the current density of 3.0 A/g in 1.0 M Na^+-PBS; (d) OER polarization curves of Co_3O_4, SC, LC and BC before (origin) and after reconstruction (Re) in 1.0 M Na^+-PBS; (e) The schematic illustration for the restructuring possibility of ABO_3 oxide in the electrolyte; (f) OER polarization curves of SC before (origin) and after reconstruction (Re) in 1.0 M K^+-PBS, the inset shows the comparison of their achieved current density at the potential of 1.75 V vs RHE; (g) Continuous potentiometric V-t measurement of SC at the current density of 3.0 A/g in 1.0 M K^+-PBS. (h) The activity comparison of SC-Re, IrO_2-origin, IrO_2-Re, and the recently reported OER catalysts in terms of the achieved current densities at 1.75 V and the needed overpotential to achieve 5.0 A/g.

be found that charge-transfer ability of SC can be improved with the treatment duration. The enhanced charge-transfer ability of SC-Re should also contribute to the highly improved OER activities of SC-Re. The 40000-s stability test over pristine SC catalyst also reveals that the required potential decreases from 1.764 V to 1.675 V vs RHE to drive a current density of 6.0 A g^{-1}, meaning that the OER activity of SC was greatly enhanced under anodic restructuring (Fig. 2c).

Interestingly, we also studied the surface change of Co_3O_4, $BaCoO_{3-\delta}$ (BC) and $LaCoO_{3-\delta}$ (LC) catalysts during the anodic conditioning in 1.0 M Na^+-PBS, and found that they experienced no significant surface restructuring (Figs. S8–S10). Their TEM-EDX mapping images have also been provided (Figs. S11 and S12). Consequently, negligible OER improvements could be observed over Co_3O_4, LC, and BC catalysts after anodic conditioning treatment (Fig. 2d, 2e). Meanwhile, the SC exhibits no significant activity enhancement after being treated in 1.0 M K^+-PBS electrolyte (Fig. 2f), because the anodic conditioning in K^+-PBS electrolyte could not initiate the surface restructuring process of SC (Fig. 2g and Fig. S13).

Noticeably, the SC-Re exhibits a remarkably high activity towards OER in 1.0 M Na^+-PBS, reaching a current density as high as 31.4 A g^{-1} at 1.75 V vs RHE. This performance is 2.1 times higher than that of IrO_2 (13.5 A g^{-1}), and 9.2 times that of IrO_2 after 12 h anodic treatment under the same conditions (2.2 A g^{-1}) (Fig. S14). We also compared the performance (*i.e.*, overpotentials at 5.0 A g^{-1} and current densities at 1.75 V vs RHE) of our catalyst against the recently reported catalysts in neutral electrolytes, such as $Ni_{0.1}Co_{0.9}P$ [30], $RuIrCaO_x$ [31], and 1-D CoHCF [32] (Fig. 2h and Table S2), and the OER activity of SC-Re is among the best-reported values. In addition, the performance of SC-Re in 1.0 M KOH is also comparable to the benchmark catalysts such as $NiCo_2S_4$ NW/NF [33] and CoS_x/Ni_3S_2@NF (Table S3) [34]. Specifically, SC-Re could achieve the current density of 65.3 A/g at 1.65 V vs RHE, 3.0 times of SC-origin (21.7 A/g), and 1.5 times of IrO_2 (43.0 A/g).

3.3. *The role of electrolyte in surface restructuring.*

To unveil the surface restructuring mechanism of SC, we compared the electrolyte compositions before and after anodic conditioning in 1.0 M Na^+-PBS and K^+-PBS electrolyte solutions at 3.0 A g^{-1} for 12 h. The

ICP-OES results reveal that there are significant amounts of Sr^{2+} ions in both electrolytes (*i.e.* 0.44 mM in used Na^+-PBS and 0.37 mM in used K^+-PBS) after the treatment (Fig. 3a), and the Sr^{2+} ion concentration in 1.0 M Na^+-PBS electrolyte is consistent with the loss amount of Sr in the SC surface as observed in EDS results (Fig. S2). The relatively high solubility of Sr in the PBS (solubility product (K_{sp}) of $SrHPO_4$ is 1.072×10^{-7}) should be the main driving force for the Sr leaching to the electrolyte [35].

More interestingly, it is found that the Na^+ ion concentration in Na^+-PBS electrolyte decreases significantly during anode conditioning, meaning that Na^+ ions could be backfilled into the SC (Fig. 3b). In contrast, the loss of K^+ ion is negligible in K^+-PBS after the anodic conditioning (Fig. S15), but the concentration of Co species in used K^+-PBS (ca. 0.054 mM Co) was clearly higher than that in Na^+-PBS (ca. 0.018 mM Co) (Fig. 3c). It indicates that the Sr^{2+} leaching could lead to the slow decomposition of the reconstructed surface of SC in K^+-PBS, exposing the unchanged inner SC crystal to the electrolyte. Therefore, the TEM image of SC after anodic conditioning in K^+-PBS shows no amorphous outer layer (Fig. S13). Instead, the observed backfilling of Na^+ in SC could help stabilize the reconstructed SC framework and restrain Co dissolution into the electrolyte and thus lead to the formation of an extended amorphous structure on the SC surface.

We postulate that the easier backfilling of Na^+ in SC than K^+ should be attributed to the smaller ionic size of Na^+. Compared to the host Sr^{2+} in SC with an ionic radius of 1.44 Å, Na^+ shows a relatively smaller radius (1.39 Å) while K^+ has an obviously larger ionic radius of 1.64 Å [36]. To better understand the roles of Na^+ and K^+ during the reconstruction of SC, we performed density functional theory (DFT) simulations to mimic the process of Na and K atoms passing a simple and respective channel caused by the leaching of Sr atom (Fig. 3d) [37,38]. We consider the passage of an atom through the [O_4] neck structure from one Sr-vacancy to another as a 5-step process with six defined states (Fig. 3e): (0) reference state with the isolated atom and the supercell; (1) entering the Sr-vacancy; (2) approaching the [O_4] neck structure; (3) locating at the center of the [O_4] neck structure; (4) moving out of the ring; (5) entering another Sr-vacancy [39]. The DFT calculations show a substantial energy decrease when the Na atom enters the channel, indicating that the introduction of the Na atom is favorable for the stability of the reconstructed structure. At the same position, the Na atom is more likely to pass through the channel

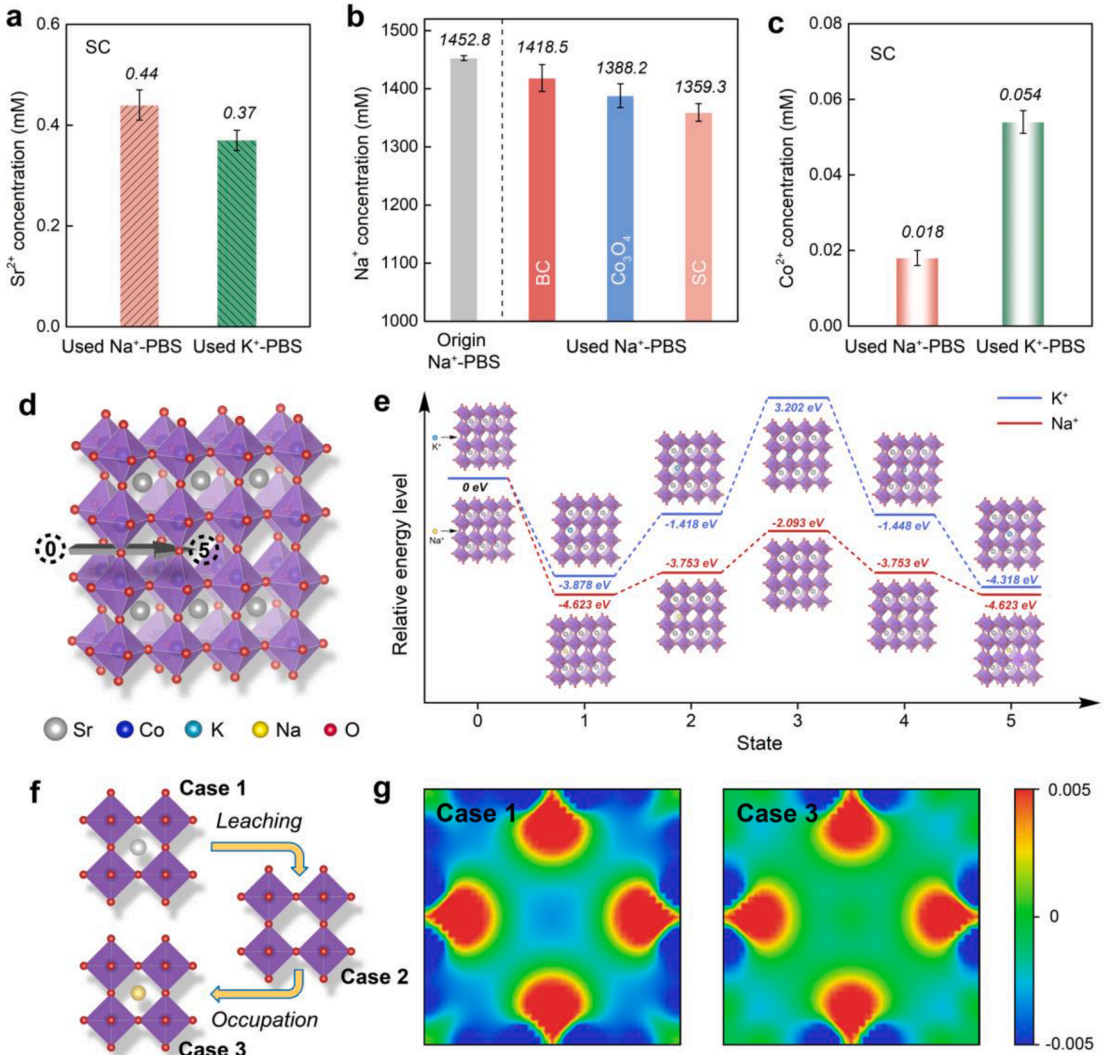

Fig. 3. (a) The Sr^{2+} concentration in the electrolyte after treating SC in 1.0 M Na^+-PBS and K^+-PBS at 3.0 A/g for 12 h; (b) The Na^+ concentration in Na^+-PBS before and after the anodic restructuring of BC, Co_3O_4, and SC; (c) The Co^{2+} concentration in the electrolyte after the anodic restructuring of SC in 1.0 M Na^+-PBS and K^+-PBS; (d) The cubic structural framework of SC supercell ($3 \times 3 \times 1$) with an artificial channel composed of three Sr-vacancies due to the leaching of Sr atoms; (e) The passage of the ions (Na^+ and K^+) through the constructed channels; (f) The schematic illustration of the leaching of Sr atom and the occupancy of Na atom in a unit cell of $SrCoO_3$; (g) The sectional charge density difference of the [O_4] neck structure for the occupancy of Sr atom (Case 1) and Na atom (Case 3) in the center of the unit cell. The charge depletion and accumulation are depicted in red and blue, respectively.

spontaneously, clearly different from the case with the K atom. Specifically, Fig. 3e shows positive relative energy for the K atom at State (3), which indicates that it is difficult for the K atom to pass through the [O_4] neck structure. The high selectivity of Na^+ over K^+ can be also observed in the experimental measurements based on an artificial sodium-selective ionic device with sub-nanometer pores, which is attributed to the size effect and molecular recognition effect [40]. To gain insight into the influence of the Na atom on the Co-O bond, we further explored the electronic structures of a unit cell of SC as shown in Fig. 3f, and compared the initial cubic structure (Case 1) to the case when the Sr-vacancy (Case 2) is occupied by the Na atom (Case 3). Charge density differences of the [O_4] neck structure for Case 1 and Case 3 are calculated by subtracting the charge density of Case 2 and corresponding atom from that of Case 1 and Case 2, respectively, as the sectional diagrams shown in Fig. 3g. We confirm that the stability of the Na-backfilled structure is much higher than that of the Sr-vacant structure, while the Co-O bond weakens (*i.e.*, benefiting the formation of oxygen vacancies) when the Sr atom is replaced by the Na atom. The Na-backfilling is likely the reason for the formation of the amorphous shell at the SC core during the restructuring process. The weakened Co-O bond could also contribute to the observed reduced Co-O coordination number from the EXAFS results (Fig. 1i).

We also studied the SC surface restructuring process at the same anodic conditioning treatment in other electrolytes with different anions such as 1.0 M Na_2CO_3/$NaHCO_3$ and 1.0 M Na_2SO_4. We noticed that these anions failed to maintain a relatively neutral local pH close to the catalyst surface during 12 h anodic conditioning (which releases protons as product), and led to the significant dissolution of the SC catalyst and even nickel support into the electrolytes.

3.4. The role of A-site cation in surface restructuring

We further studied the role of A-site cations in the surface restructuring processes over Co_3O_4 and BC catalysts during the anodic conditioning (Fig. 3b). The absence of the Sr in the Co_3O_4 led to negligible surface restructuring after 12 h anodic conditioning in Na^+-PBS (Fig. S8), and no Co species was detected in the used electrolyte. In addition, the negligible surface restructuring on BC (Fig. S9) should be attributed to the low solubility of barium phosphate (K_{sp} = 3.40 × 10^{-23}) that limits the dissolution of the A-site cations. The limited Ba^{2+} dissolution can be confirmed by the ICP-OES results that there is a much lower concentration of Ba^{2+} (ca. 0.11 mM) as compared to Sr^{2+} for SC (ca. 0.44 mM) in the Na^+-PBS. This result indicates that the Sr^{2+} dissolution is one of the main drivers for the surface restructuring and causes the Co^{2+} leaching in SC. After 12 h anode conditioning, the content of Na^+ remained almost unchanged for both Co_3O_4 and BC samples, further confirming that Sr dissolution is essential for the Na^+ backfilling in SC.

The electrochemical conditions should also play a role in facilitating the SC surface restructuring. We treated the SC catalysts in Na^+-PBS electrolyte using three different current densities while maintaining the same passage quantity of total charge. There was no clear trend spotted from HR-TEM images of the structural evolution over the SC particles (Fig. S16). Similarly, there are no obvious correlations between the treatment conditions and dissolution of the Sr and Co species in the electrolyte, suggesting that the Sr dissolution is not initiated by the electrochemical conditioning (Table S4). Instead, the Sr dissolution is likely driven by the Sr concentration gradient across the catalyst-electrolyte interfaces. However, the concentrations of Na^+ in the electrolyte are similar for the three current densities, meaning that the Na^+ backfilling is correlated to the total charges transferred in the reactions (Table S4). We also found that immersing SC in the Na^+-PBS with no charge transferred could not induce noticeable surface restructuring (Fig. S17).

3.5. The effect of surface restructuring on the OER intrinsic activity

To examine the role of the surface reconstruction on the OER intrinsic activity of the active sites, we compared the activity of SC before and after surface reconstructions in 0.0316 M, 0.1 M, 0.316 M, and 1.0 M Na^+-PBS electrolytes. Fig. 4a–4c presents obvious dependency of the OER activity over the Na^+-PBS concentration, confirming the contribution of Na^+-PBS to the OER catalysis over both original and restructured SC oxides. Interestingly, evidenced by its smaller slope, the SC-Re should have a lower OER dependency over Na^+-PBS concentration than the original analogue, meaning that the effect of the Na^+-PBS concentration is weakened after the development of the core–shell structure. We believe the phenomenon is related to the aforementioned steric hindrance of the thick amorphous shell that limits further electrolyte penetration and SC/electrolyte interfacial interactions. The lower OER dependency on Na^+-PBS could be attributed to the enhanced proton transfer process by the incorporation of phosphate, which was previously reported for (La, Sr)CoO_3 with the surface-modified with phosphate [41]. Our results of the density-functional theory (DFT) calculation further confirm that phosphate could also lower the activation energy by 0.19 eV by accelerating the proton removal from H_2O and HO* intermediate, where * represents the adsorption site at SC surface (Figs. S18 and S19) [42,43].

Furthermore, we observe a stronger pH dependency of OER activities over SC-Re than over the SC-origin in KOH electrolytes (Fig. 4d-4f). A high pH dependency indicates the participation of the lattice oxygen in the OER catalysis, where lattice oxygen vacancy is the essential ingredient [18,44]. The surface reconstruction process can create surface oxygen vacancies to strengthen intermediate adsorption and tether the surface with phosphate to accelerate proton transfer, jointly enhancing the overall OER reactivity [45]. This proposed controllable catalyst/electrolyte cations matching-induced restructuring strategy can be a more effective pathway to achieve a high electrochemical activity compared with the conventional surface restructuring in alkaline solution. After reconstruction in 1.0 M Na^+-PBS, the SC-Re even shows a remarkably higher OER activity compared with the SC-origin in 1.0 M KOH (Fig. 4g). To achieve the mass current density of 100.0 A/g, SC-Re needs only an overpotential of 385 mV, clearly lower than that of SC-origin (494 mV, Fig. 4f). In contrast, the reconstructed SC sample in 1.0 M KOH and 1.0 M NaOH can only induce minor activity enhancement, which needs 491 mV and 450 mV, respectively, to achieve 100 A/g (Fig. 4h).

We tested the single-chamber full cell water electrolysis in pH-neutral 1.0 M Na^+-PBS electrolyte by applying the SC-Re as the anode catalyst and Pt-loaded carbon black (Pt/C) as the catalyst to evolve hydrogen (Fig. S20a). The SC-re-based cell achieved a current density of 28.8 A g^{-1} at an overall cell voltage of 2.2 V, outperforming the RuO_2-based equivalent (4.1 A g^{-1} at 2.2 V) by almost seven-folds (Fig. S20b, c). We also assembled a 5.0 cm^2 SC-Re electrode into an AEMWE, where the Pt/C catalyst deposited on Ti foam serves as the cathode and the Sustainion X37-50 Grade T as the anion exchange membrane (Fig. S20d). This cell can achieve a current density of 90.7 A g^{-1} at an overall cell voltage of 2.2 V (Fig. S20e), and the gas chromatograph results as shown in Fig. S21 confirmed that the products of the cell are H_2 and O_2. No CO and CO_2 were detected (precision: ppm). This cell can produce 1.8 ± 0.2 mL min^{-1} O_2 gas and 3.9 ± 0.2 mL min^{-1} (Fig. S20f), and therefore faradaic efficiency for OER and HER are both ~100 %. The stability test of SC-Re ‖ Pt/C at 85.0 A g^{-1} shows negligible degradation for 24 h (Fig. S22). These results demonstrated the potential of the SC-Re to be applied in a large-scale water electrolyzer.

3.6. Proposed surface restructuring mechanism

Based on the results of the controlling experiment, we could safely conclude that the surface restructuring of SC during anodic conditioning involves the dissolution of A-site cations and backfilling of electrolyte

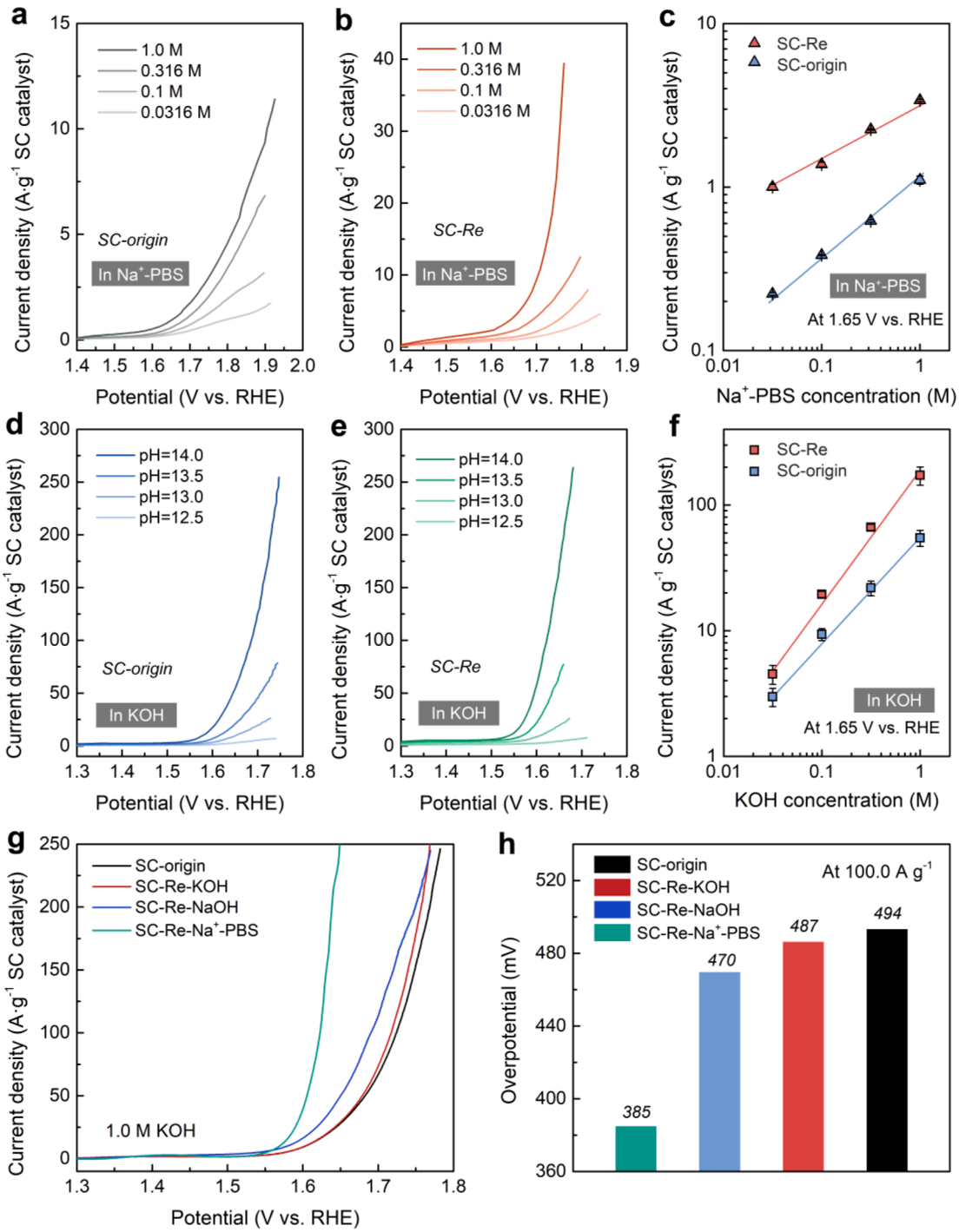

Fig. 4. (a, b) OER polarization curves of (a) SC-origin and (b) SC-Re in Na^+-PBS of 0.0316 M, 0.1 M, 0.316 M and 1.0 M; (c) OER current densities of SC-origin and SC-Re at 1.65 V vs RHE that plotted to show their correlation with Na^+-PBS concentration; (d, e) OER polarization curves of (d) SC-origin and (e) SC-Re in KOH of pH = 12.5, 13.0, 13.5 and 14.0; (f) OER current densities of SC-origin and SC-Re at 1.65 V vs RHE that plotted to show their correlation with KOH concentration; (g) OER polarization curves in 1.0 M KOH of SC-origin and SC-Re samples that treated in 1.0 M KOH, 1.0 M NaOH, and 1.0 M Na^+-PBS; (h) The overpotential needed to achieve the current density of 100.0 A/g in 1.0 M KOH for SC-origin and different SC-Re samples.

cations (Fig. 5a). This restructuring process mainly arises from (1) the solubility of A-site cations in the electrolyte, (2) the size of electrolyte ions, and (3) the charge transfer process. The solubility of the catalyst cation determines the concentration gradient across the catalyst-electrolyte interface, which drives the catalyst dissolution into the electrolyte. The catalyst dissolution together with anodic conditioning charge transfer enables the backfilling of Na^+ in the electrolyte to the vacant Sr site and subsequently stabilizes the B-site cobalt structures at the SC surface. The slightly higher cobalt oxidation states as observed from the XAS results should be attributed to the Sr-Na swap on the SC surface that causes the reduction of A-site cation valence and the electrochemical oxidation during the anodic treatment (Fig. 1g, h). Meanwhile, the exchange between Sr and Na could be associated with the formation of oxygen vacancies (as evidenced by the reduced Co-O coordination numbers) and phosphate incorporation (as evidenced by the featured XAFS spectra of Co-phosphate (Fig. 1i) and FTIR characteristic

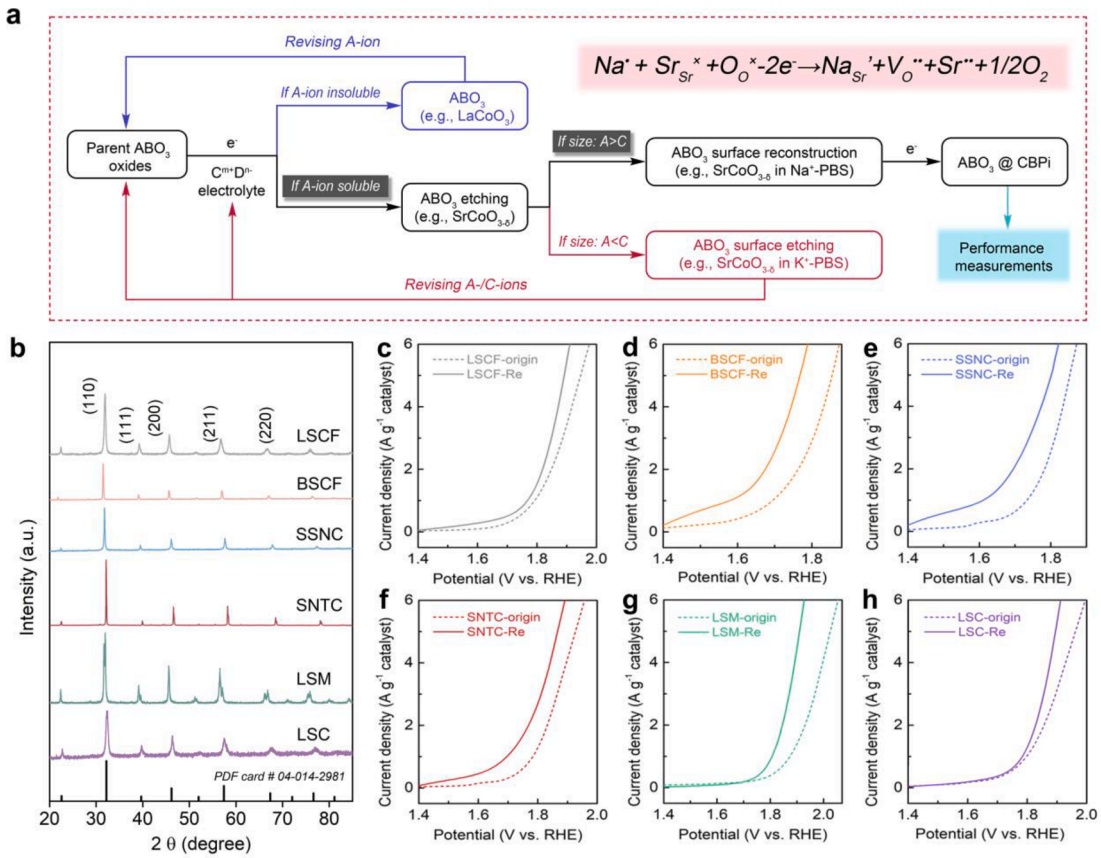

Fig. 5. (a) The schematic illustration for the restructuring possibility of ABO_3 oxide in the electrolyte; (b) XRD patterns of LSC, LSM, SNTC, SSNC, BSCF, and LSCF; OER polarization curves of (c) LSCF, (d) BSCF, (e) SSNC, (f) SNTC, (g) LSM, and (h) LSC before (origin) and after reconstruction (Re) in 1.0 M Na^+-PBS.

peak for phosphate (Fig. S3). The induced charge imbalance, like other perovskite metal oxides [46], could also create oxygen vacancies with each carrying two positive charges, as depicted by the equation (inset in Fig. 5a). Therefore, the negatively charged oxygen ions from phosphate could interact with the positively charged oxygen vacancies on the surface, resulting in the adsorption of phosphate in the surface shell lattice.

The surface restructuring process in Na^+-PBS can be a general restructuring pathway for the ABO_3 materials that meet the rules described in Fig. 5a, and could effectively enhance the OER activity. To demonstrate its generality, we prepared a few Sr-containing cubic perovskites, including $La_{0.6}Sr_{0.4}CoO_{3-\delta}$ (LSC), $La_{0.6}Sr_{0.4}MnO_{3-\delta}$ (LSM), $La_{0.5}Sr_{0.5}Co_{0.8}Fe_{0.2}O_{3-\delta}$ (LSCF), $Ba_{0.5}Sr_{0.5}Co_{0.8}Fe_{0.2}O_{3-\delta}$ (BSCF), $SrSc_{0.175}Nb_{0.025}Co_{0.8}O_{3-\delta}$ (SSNC), and $SrNb_{0.1}Ta_{0.1}Co_{0.8}O_{3-\delta}$ (SNTC) catalysts, and compared the OER reactivity in 1.0 M Na^+-PBS before and after anodic treatment for 12 h at 3.0 A g^{-1}. Their XRD patterns are shown in Fig. 5b. All these materials show discernible enhancement of the OER activity after the anodic treatment. The overpotential to achieve a current density of 3.0 A g^{-1} is reduced by 70 mV for LSCF, 125 mV for BSCF, 50 mV for SSNC, 68 mV for SNTC, 130 mV for LSM, and 86 mV for LSC. (Fig. 5c–5 h). This result further confirms the important role of pairing cathode cations (Sr^{2+}) with electrolyte cations (Na^+) in improving OER activity via surface restructuring.

4. Conclusions

To conclude, we report a novel *operando* surface restructuring pathway, highlighting the important role of pairing cations in catalyst and electrolyte in the electrochemical surface restructuring process. In our study, we use the $SrCoO_{3-\delta}$ perovskite as the model catalyst to evolve oxygen from water in the Na^+-PBS electrolyte and study the effect of surface restructuring in enhancing OER catalytic activity. We find that the surface restructuring process requires the dissolution of soluble A-site cation (Sr) to the electrolyte, backfilling of small electrolyte cations (Na^+) to large A-site vacancy in the catalyst lattice, and anion (phosphate) incorporation. Through both experimental and theoretical studies, we confirm that the A-site cation dissolution is driven by the concentration gradient across the catalyst-electrolyte interface, and this dissolution process together with the anodic polarization initiates electrolyte ion backfilling and incorporation. Consequently, the surface restructuring leads to the formation of an amorphous shell with a thickness of ten of nanometers at the catalyst/electrolyte interfaces. This shell structure is highly active in OER catalysis due to the created lattice oxygen vacancies that strengthen intermediate adsorption and incorporate phosphate that accelerate proton transfer. Overall, this work highlights the important roles of the cations in both the catalyst and electrolyte in determining the electrode–electrolyte interactions during electrocatalysis. We anticipate this work to offer alternative strategies to advance electrochemical applications such as water and CO_2 electrolysis via optimizing the catalyst compositional chemistry with properties of electrolyte.

Declaration of Competing Interest

The authors declare that they have no known competing financial interests or personal relationships that could have appeared to influence the work reported in this paper.

Data availability

Data will be made available on request.

Acknowledgements

L. Z. and Z. L. contributed equally to this work. Z. Z. likes to thank the financial support from Australian Research Council Discovery Projects (DP190101782) and (DP200101397). The authors thank the valuable advice from Prof. Honglai Liu about the DFT calculation. The authors also thank the Shanghai Synchrotron Radiation Facility (BL14W1, SSRF) for XAS equipment access.

Appendix A. Supplementary data

Supplementary data to this article can be found online at https://doi.org/10.1016/j.cej.2022.140071.

References

[1] Z.N. Zahran, E.A. Mohamed, Y. Tsubonouchi, M. Ishizaki, T. Togashi, M. Kurihara, K. Saito, T. Yui, M. Yagi, Electrocatalytic water splitting with unprecedentedly low overpotentials by nickel sulfide nanowires stuffed into carbon nitride scabbards, Energy Environ. Sci. 14 (10) (2021) 5358–5365.
[2] C.L. Bentley, M. Kang, P.R. Unwin, Nanoscale surface structure-activity in electrochemistry and electrocatalysis, J. Am. Chem. Soc. 141 (6) (2019) 2179–2193.
[3] J. Bao, X. Zhang, B.o. Fan, J. Zhang, M. Zhou, W. Yang, X. Hu, H. Wang, B. Pan, Y. i. Xie, Ultrathin spinel-structured nanosheets rich in oxygen deficiencies for enhanced electrocatalytic water oxidation, Angew. Chem. Int. Ed. 54 (25) (2015) 7399–7404.
[4] L. Zhuang, Y. Jia, H. Liu, X. Wang, R.K. Hocking, H. Liu, J. Chen, L. Ge, L. Zhang, M. Li, C.L. Dong, Y.C. Huang, S. Shen, D. Yang, Z. Zhu, X. Yao, Defect-induced Pt-Co-Se coordinated sites with highly asymmetrical electronic distribution for boosting oxygen-involving electrocatalysis, Adv. Mater. 31 (2019) 1805581.
[5] X. Xiao, L. Zou, H. Pang, Q. Xu, Synthesis of micro-nanoscaled metal-organic frameworks and their direct electrochemical applications, Chem. Soc. Rev. 49 (2020) 301–331.
[6] F. Chen, Z. Wu, Z. Adler, H. Wang, Stability challenges of electrocatalytic oxygen evolution reaction: from mechanistic understanding to reactor design, Joule 5 (2021) 1704–1731.
[7] J. Wang, S.-J. Kim, J. Liu, Y. Gao, S. Choi, J. Han, H. Shin, S. Jo, J. Kim, F. Ciucci, H. Kim, Q. Li, W. Yang, X. Long, S. Yang, S.-P. Cho, K.H. Chae, M.G. Kim, H. Kim, J. Lim, Redirecting dynamic surface restructuring of a layered transition metal oxide catalyst for superior water oxidation, Nat. Catal. 4 (3) (2021) 212–222.
[8] J. Li, C.A. Triana, W. Wan, D.P. Adiyeri Saseendran, Y. Zhao, S.E. Balaghi, S. Heidari, G.R. Patzke, Molecular and heterogeneous water oxidation catalysts: recent progress and joint perspectives, Chem. Soc. Rev. 50 (4) (2021) 2444–2485.
[9] Z. Lu, G. Chen, Y. Li, H. Wang, J. Xie, L. Liao, C. Liu, Y. Liu, T. Wu, Y. Li, A.C. Luntz, M. Bajdich, Y.i. Cui, Identifying the active surfaces of electrochemically tuned $LiCoO_2$ for oxygen evolution reaction, J. Am. Chem. Soc. 139 (17) (2017) 6270–6276.
[10] L.C. Seitz, C.F. Dickens, K. Nishio, Y. Hikita, J. Montoya, A. Doyle, C. Kirk, A. Vojvodic, H.Y. Hwang, J.K. Norskov, T.F. Jaramillo, A highly active and stable $IrO_x/SrIrO_3$ catalyst for the oxygen evolution reaction, Science 353 (6303) (2016) 1011–1014.
[11] D. Guan, G. Ryu, Z. Hu, J. Zhou, C. Dong, Y. Huang, K. Zhang, Y. Zhong, A. C. Komarek, M. Zhu, X. Wu, C. Pao, C. Chang, H. Lin, C. Chen, W. Zhou, Z. Shao, Utilizing ion leaching effects for achieving high oxygen-evolving performance on hybrid nanocomposite with self-optimized behaviors, Nat. Commun. 11 (2020) 3376.
[12] T. Wu, S. Sun, J. Song, S. Xi, Y. Du, B.o. Chen, W.A. Sasangka, H. Liao, C.L. Gan, G. G. Scherer, L. Zeng, H. Wang, H. Li, A. Grimaud, Z.J. Xu, Iron-facilitated dynamic active-site generation on spinel $CoAl_2O_4$ with self-termination of surface reconstruction for water oxidation, Nat. Catal. 2 (9) (2019) 763–772.
[13] H. Jiang, Q. He, X. Li, X. Su, Y. Zhang, S. Chen, S. Zhang, G. Zhang, J. Jiang, Y. Luo, P.M. Ajayan, L. Song, Tracking structural self-reconstruction and identifying true active sites toward cobalt oxychloride precatalyst of oxygen evolution reaction, Adv. Mater. 31 (2019) 1805127.
[14] H.N. Nong, T. Reier, H.-S. Oh, M. Gliech, P. Paciok, T.H.T. Vu, D. Teschner, M. Heggen, V. Petkov, R. Schlögl, T. Jones, P. Strasser, A unique oxygen ligand environment facilitates water oxidation in hole-doped $IrNiO_x$ core–shell electrocatalysts, Nat. Catal. 1 (11) (2018) 841–851.
[15] Á. Vass, B. Endrődi, G.F. Samu, Á. Balog, A. Kormányos, S. Cherevko, C. Janáky, Local chemical environment governs anode processes in CO_2 electrolyzers, ACS Energy Lett. 6 (11) (2021) 3801–3808.
[16] D. Gao, R.M. Arán-Ais, H.S. Jeon, B. Roldan Cuenya, Rational catalyst and electrolyte design for CO_2 electroreduction towards multicarbon products, Nat. Catal. 2 (3) (2019) 198–210.
[17] Y. Pi, Y. Xu, L. Li, T. Sun, B. Huang, L. Bu, Y. Ma, Z. Hu, C.W. Pao, X. Huang, Selective surface reconstruction of a defective iridium-based catalyst for high-efficiency water splitting, Adv. Funct. Mater. 30 (2020) 2004375.
[18] J. Hwang, R.R. Rao, L. Giordano, Y.u. Katayama, Y. Yu, Y. Shao-Horn, Perovskites in catalysis and electrocatalysis, Science 358 (6364) (2017) 751–756.
[19] H.S. Ahn, T.D. Tilley, Electrocatalytic Water oxidation at neutral pH by a Nanostructured $Co(PO_3)_2$ Anode, Adv. Funct. Mater. 23 (2) (2013) 227–233.
[20] Y. Shao, X. Xiao, Y.-P. Zhu, T.-Y. Ma, Single-crystal cobalt phosphate nanosheets for biomimetic oxygen evolution in neutral electrolytes, Angew. Chem. Int. Ed. 58 (41) (2019) 14599–14604.
[21] Y. Zhu, W. Zhou, J. Sunarso, Y. Zhong, Z. Shao, Phosphorus-doped perovskite oxide as highly efficient water oxidation electrocatalyst in alkaline solution, Adv. Funct. Mater. 26 (32) (2016) 5862–5872.
[22] E. Fabbri, M. Nachtegaal, T. Binninger, X.i. Cheng, B.-J. Kim, J. Durst, F. Bozza, T. Graule, R. Schäublin, L. Wiles, M. Pertoso, N. Danilovic, K.E. Ayers, T. J. Schmidt, Dynamic surface self-reconstruction is the key of highly active perovskite nano-electrocatalysts for water splitting, Nat. Mater. 16 (9) (2017) 925–931.
[23] X. Li, H. Wang, Z. Cui, Y. Li, S. Xin, J. Zhou, Y. Long, C. Jin, J.B. Goodenough, Exceptional oxygen evolution reactivities on $CaCoO_3$ and $SrCoO_3$, Sci. Adv. 5 (2019) eaav6262.
[24] D. Chen, S. Nie, L. Wu, X. Zheng, S. Du, X. Duan, Q. Niu, P. Zhang, S. Dai, Metal-tannin coordination assembly route to nanostructured high-entropy oxide perovskites with abundant defects, Chem. Mater. 34 (4) (2022) 1746–1755.
[25] M. Li, M. Zhao, F. Li, W. Zhou, V.K. Peterson, X. Xu, Z. Shao, I. Gentle, Z. Zhu, A niobium and tantalum co-doped perovskite cathode for solid oxide fuel cells operating below 500 degrees C, Nat. Commun. 8 (2017) 13990.
[26] S. Nie, L. Wu, L. Zhao, P. Zhang, Enthalpy-change driven synthesis of high-entropy perovskite nanoparticles, Nano Res. 15 (6) (2022) 4867–4872.
[27] L. Zhuang, L. Ge, H. Liu, Z. Jiang, Y. Jia, Z. Li, D. Yang, R.K. Hocking, M. Li, L. Zhang, X. Wang, X. Yao, Z. Zhu, Ultrathin two-dimensional metal-organic framework nanosheets for the oxygen evolution reaction, Angew. Chem. Int. Ed. 58 (2019) 13565–13572.
[28] Q. Lu, S. Huberman, H. Zhang, Q. Song, J. Wang, G. Vardar, A. Hunt, I. Waluyo, G. Chen, B. Yildiz, Bi-directional tuning of thermal transport in $SrCoO_x$ with electrochemically induced phase transitions, Nat. Mater. 19 (6) (2020) 655–662.
[29] M.W. Kanan, J. Yano, Y. Surendranath, M. Dincă, V.K. Yachandra, D.G. Nocera, Structure and valency of a cobalt-phosphate water oxidation catalyst determined by in situ X-ray spectroscopy, J. Am. Chem. Soc. 132 (39) (2010) 13692–13701.
[30] R. Wu, B. Xiao, Q. Gao, Y.-R. Zheng, X.-S. Zheng, J.-F. Zhu, M.-R. Gao, S.-H. Yu, A Janus nickel cobalt phosphide catalyst for high-efficiency neutral-pH water splitting, Angew. Chem. Int. Ed. 57 (47) (2018) 15445–15449.
[31] L. Zhang, L. Wang, Y. Wen, F. Ni, B. Zhang, H. Peng, Boosting neutral water oxidation through surface oxygen modulation, Adv. Mater. 32 (2020) 2002297.
[32] H.T. Bui, D.Y. Ahn, N.K. Shrestha, M.M. Sung, J.K. Lee, S.-H. Han, Self-assembly of cobalt hexacyanoferrate crystals in 1-D array using ion exchange transformation route for enhanced electrocatalytic oxidation of alkaline and neutral water, J. Mater. Chem. A 4 (25) (2016) 9781–9788.
[33] A. Sivanantham, P. Ganesan, S. Shanmugam, Hierarchical $NiCo_2S_4$ nanowire arrays supported on ni foam: an efficient and durable bifunctional electrocatalyst for oxygen and hydrogen evolution reactions, Adv. Funct. Mater. 26 (2016) 4661–4672.
[34] S. Shit, S. Chhetri, W. Jang, N.C. Murmu, H. Koo, P. Samanta, T. Kuila, Cobalt sulfide/nickel sulfide heterostructure directly grown on nickel foam: an efficient and durable electrocatalyst for overall water splitting application, ACS Appl. Mater. Interfaces 10 (2018) 27712–27722.
[35] Y.-J. Shih, H.-C. Chang, Y.-H. Huang, Reclamation of phosphorus from aqueous solutions as alkaline earth metal phosphate in a fluidized-bed homogeneous crystallization (FBHC) process, J. Taiwan Inst. Chem. E. 62 (2016) 177–186.
[36] S.F. Matar, G. Campet, M.A. Subramanian, Electronic properties of oxides: chemical and theoretical approaches, Prog. Solid State Ch. 39 (2) (2011) 70–95.
[37] H. Tao, C. Lian, H. Liu, Multiscale modeling of electrolytes in porous electrode: from equilibrium structure to non-equilibrium transport, Green Energy Environ 。5 (2020) 303–321.
[38] H. Tao, G. Chen, C. Lian, H. Liu, M.-O. Coppens, Multiscale modelling of ion transport in porous electrodes, AIChE J. 68 (2022) e17571.
[39] H. Li, C. Qiu, S. Ren, Q. Dong, S. Zhang, F. Zhou, X. Liang, J. Wang, S. Li, M. Yu, Na$^+$-gated water-conducting nanochannels for boosting CO_2 conversion to liquid fuels, Science 367 (2020) 667–671.
[40] T. Ye, G. Hou, W. Li, C. Wang, K. Yi, N. Liu, J. Liu, S. Huang, J. Gao, Artificial sodium-selective ionic device based on crown-ether crystals with subnanometer pores, Nat. Commun. 12 (2021) 5231.
[41] C. Yang, C. Laberty-Robert, D. Batuk, G. Cibin, A.V. Chadwick, V. Pimenta, W. Yin, L. Zhang, J.-M. Tarascon, A. Grimaud, Phosphate ion functionalization of perovskite surfaces for enhanced oxygen evolution reaction, J. Phys. Chem. Lett. 8 (15) (2017) 3466–3472.
[42] X. Xu, Y. Pan, Y. Zhong, C. Shi, D. Guan, L. Ge, Z. Hu, Y. Chin, H. Lin, C. Chen, H. Wang, S. Jiang, Z. Shao, New undisputed evidence and strategy for enhanced lattice-oxygen participation of perovskite electrocatalyst through cation deficiency manipulation, Adv. Sci. 9 (2022) 2200530.
[43] J. Liu, J. Xie, R. Wang, B. Liu, X. Meng, X. Xu, B. Tang, Z. Cai, J. Zou, Interfacial electron modulation of Cu_2O by Co_3O_4 embedded in hollow carbon cube skeleton for boosting oxygen reduction/revolution reactions, Chem. Eng. J. 450 (2022), 137961.
[44] A. Grimaud, O. Diaz-Morales, B. Han, W.T. Hong, Y.-L. Lee, L. Giordano, K. A. Stoerzinger, W.T. Hong, M.T.M. Koper, Y. Shao-Horn, Activating lattice oxygen

redox reactions in metal oxides to catalyse oxygen evolution, Nat. Chem. 9 (2017) 457–465.
[45] B. Han, K. Stoerzinger, V. Tileli, A. Gamalski, E. Stach, Y. Shao-Horn, Nanoscale structural oscillations in perovskite oxides induced by oxygen evolution, Nat. Mater. 16 (1) (2017) 121–126.
[46] A.U. Rehman, M. Li, R. Knibbe, M.S. Khan, V.K. Peterson, H.E.A. Brand, Z. Li, W. Zhou, Z. Zhu, Enhancing oxygen reduction reaction activity and CO_2 tolerance of cathode for low-temperature solid oxide fuel cells by in situ formation of carbonates, ACS Appl. Mater. Inter. 11 (30) (2019) 26909–26919.